Surfaces and Interfaces 38 (2023) 102808

Contents lists available at ScienceDirect

Surfaces and Interfaces

journal homepage: www.sciencedirect.com/journal/surfaces-and-interfaces

Interfacial self-assembled dual-functional nanocomposite films for SERS monitoring of visible-light photocatalytic degradation of organic dye pollutants

Wanling Chen [a], Wanlin Wang [b], Hongyun Xing [b], Wan Li [a], Haiwei He [a,c], Wei Li [a], Paul K. Chu [d], Guofen Song [a,*], Huaiyu Wang [a,c,*], Penghui Li [a,c,*]

[a] Institute of Biomedicine and Biotechnology, Shenzhen Institute of Advanced Technology, Chinese Academy of Sciences, Shenzhen 518055, China
[b] College of Electronics and Information Engineering, Shenzhen University, Shenzhen, 518060, China
[c] University of Chinese Academy of Sciences, Beijing 100049, China
[d] Department of Physics, Department of Materials Science and Engineering, and Department of Biomedical Engineering, City University of Hong Kong, Tat Chee Avenue, Kowloon, Hong Kong, China

ARTICLE INFO

Keywords:
Self-assembled nanocomposites
SERS
Monitoring
Photocatalytic degradation
Organic dyes pollutants

ABSTRACT

Photocatalytic degradation by visible-light responsive photocatalysts is an efficient strategy to treat organic dye pollutants and monitoring of the photocatalytic reaction mechanisms and kinetics is important to the design of high-performance photocatalysts. Herein, a dual-functional graphitic carbon nitride/gold nanoparticles (g-C_3N_4/AuNPs) nanocomposite film is introduced to monitor the photocatalytic reactions by surface-enhanced Raman scattering (SERS) while degrading organic dyes photocatalytically. The nanocomposite film fabricated by two-step interfacial self-assembly consists of orderly arranged g-C_3N_4 film anchored on a closely packed AuNPs monolayer film. The nanoplatform has excellent SERS characteristics such as a rhodamine 6G (R6G) detection limit of 8.8×10^{-10} M, and good SERS detection uniformity with a relative standard deviation (RSD) of 9.62%, which is crucial to quantitative determination and accurate monitoring of the photocatalytic reactions. The nanoplatform is employed in visible-light photocatalytic degradation of organic dyes including R6G, methylene blue, acid orange II, and acid orange 74. The reactions follow the pseudo-first-order kinetics as revealed by SERS and the photocatalytic degradation mechanism is postulated to be the promoted charge separation. The results reveal a high-performance dual-functional nanoplatform suitable for visible-light photocatalytic degradation of organic dye pollutants and SERS monitoring of the reactions.

1. Introduction

Organic dye pollutants produced by the textile, clothing and printing industry are not only detrimental to public health, but also damage the ecosystem, and efforts have been made to solve the problem [1]. Photocatalytic degradation of organic dyes has developed to be one of the promising pollution control technologies due to the high efficiency, mild reaction conditions, simplicity, and environmental benign [2], and visible-light responsive photocatalysis is especially attractive because it can realize the utilization and transformation of clean solar energy [3]. Generally, active visible-light photocatalysts that have high intrinsic adsorption in the visible light region are a requisite in visible-light responsive photocatalysis. Graphitic carbon nitride (g-C_3N_4), a polymeric two-dimensional semiconductor, is a rising star among the visible-light photocatalysts because of the tunable bandgap, visible light absorption, excellent chemical stability, low cost, as well as the large surface area [4,5]. However, the recombination of photogenerated electron-hole pairs in pristine g-C_3N_4 affects the photocatalytic performance and the recombination rate must be restrained. Therefore, there is high demand in developing g-C_3N_4-based composite photocatalysts and constructing heterojunctions, to reduce electron-hole pair recombination and achieve superior visible-light photocatalytic effect [6].

In addition to degradation, monitoring of the photocatalytic reactions is crucial to elucidating the mechanisms and kinetics as well as design of high-performance photocatalysts [7]. Surface-enhanced Raman scattering (SERS) can impart vibrational information with high

* Corresponding authors:
E-mail addresses: gf.song@siat.ac.cn (G. Song), hy.wang1@siat.ac.cn (H. Wang), ph.li@siat.ac.cn (P. Li).

https://doi.org/10.1016/j.surfin.2023.102808
Received 12 January 2023; Received in revised form 1 March 2023; Accepted 7 March 2023
Available online 16 March 2023

efficiency and sensitivity by taking advantage of the enhanced Raman signals arising from localized surface plasmon resonance (LSPR), typically on metallic nanostructures [8]. In fact, SERS has exhibited remarkable capability of photocatalysis analysis, such as bond formation analysis [9,10], catalytic sites locating [11,12], and intermediate species identification [13,14], thus is a fully competent in the photocatalytic degradation reaction monitoring.

Applying SERS to the monitoring of photocatalytic reactions requires the development of a dual-functional platform that is both plasmonically and catalytically active, to simultaneously realize the photocatalytic reaction stimulation and Raman signals enhancement. In this respect, nanocomposites consisting of noble metal nanoparticles and semiconductors are attractive [15,16]. On one hand, these nanocomposites exhibit elevated photocatalytic activity because of efficient separation and transfer of photogenerated charges as a result of the potential difference between the metal nanoparticles and semiconductors [17]. On the other hand, the SERS performance is augmented by the combination of electromagnetic enhancement endowed by metallic plasmonic resonance as well as chemical enhancement stemming from the interactions and charge transfer between semiconductors and molecules [18]. Hence, introduction of noble metal nanoparticles to g-C_3N_4-based visible-light photocatalytic degradation system is a viable strategy to realize SERS monitoring of photocatalytic reactions. However, disordered nanocomposites in forms of random clusters or aggregates tend to exhibit large deviation in their SERS signal intensity and this non-uniformity negatively affects the detection reproducibility and quantitative determination [19], leading to inaccurate analysis and incomplete information about the reactions. Fortunately, self-assembled ordered nanostructures can offer homogeneous distributed SERS "hot spots", rendering the SERS detection with high sensitivity and reproducibility [20,21].

Herein, a self-assembled nanocomposite film comprising g-C_3N_4 nanosheets and AuNPs is designed and demonstrated as a dual-functional platform for both photocatalytic degradation of organic dyes and SERS monitoring of the degradation reactions. The g-C_3N_4/AuNPs nanocomposite film consisting of orderly arranged g-C_3N_4 film on a closely packed AuNPs monolayer film is fabricated by liquid-liquid interfacial self-assembly and pattern transfer. The ordered structure not only contributes to the uniform distribution of "hot spots" for sensitive and reproducible SERS detection [22,23], but also facilitates the uniform formation of active sites for photocatalytic reaction. The SERS enhancement can be attributed to a combination of electromagnetic enhancement and chemical enhancement. More excitingly, the photocatalysis activity evaluation and reaction kinetics investigation can be achieved by SERS monitoring with the nanocomposite film in photocatalytic degradation of R6G and other organic dyes, and the photocatalytic mechanism is proposed. The results reveal a nanocomposite film platform and efficient technique for photocatalytic degradation of organic dye pollutants and SERS monitoring of the reactions.

2. Experimental section

2.1. Materials

Hexadecyl trimethyl ammonium bromide (CTAB), sodium hydroxide (NaOH), ascorbic acid (AA), polyvinylpyrrolidone (PVP, K30), nitric acid (HNO_3), ethanol, dichloromethane, *n*-hexane, rhodamine 6G (R6G) and methylene blue were bought from Sinopharm Chemical Reagent Co. Ltd. (Shanghai, China). Chloroauric acid ($HAuCl_4{\cdot}4H_2O$, 99.99%), melamine, acid orange II and acid orange 74 were purchased from Aladdin Reagents (Shanghai, China) and sodium borohydride ($NaBH_4$) was obtained from Sigma-Aldrich Co. (St Louis, USA). All the chemicals were used as received without further purification and Millipore™ Milli-Q water (resistivity >18 MΩ/cm at 25°C) was used throughout the experiments.

2.2. Preparation and ligand exchange of AuNPs

The CTAB coated AuNPs (CTAB-AuNPs) were prepared by a seed-mediated method at room temperature [24]. Firstly, fresh ice-cold $NaBH_4$ (10 mM, 620 μL) was added into the mixture of CTAB (0.2 M, 5 mL), H_2O (4.5 mL), and $HAuCl_4{\cdot}4H_2O$ (5 mM, 500 μL), and vigorously stirred for 2 min, to obtain the gold seed solution. Then, $HAuCl_4{\cdot}4H_2O$ (5 mM, 12 mL) and NaOH (1 M, 300 μL) were added to CTAB (0.2 M, 60 mL), followed by the addition of AA (10 mM, 8 mL), and gently stirred until the solution became colorless. Afterwards, 120 μL of the gold seed solution were introduced rapidly to the above solution and sat for 3 h under 37°C. The solution was centrifuged at 11,000 rpm for 15 min, and the precipitate was re-dispersed in 80 mL H_2O, obtaining the CTAB-AuNPs solution.

To perform ligand exchange for the AuNPs, 30 mL of the CTAB-AuNPs solution were subjected to centrifugation, and the precipitate was re-dispersed in 30 mL of the PVP solution (1 wt% in ethanol) by stirring for 1 h. The solution was then centrifuged at 11,000 rpm for 15 min, and the obtained PVP-AuNPs precipitate was washed with ethanol, centrifuged and re-dispersed in 3 mL of ethanol, and stored at 4°C before use.

2.3. Preparation of g-C_3N_4 nanosheets

The bulk g-C_3N_4 was synthesized by polymerizing melamine in a muffle furnace at a high temperature. 30 g of melamine were placed in the muffle furnace and the temperature was raised to 550°C at a ramping rate of 5°C min^{-1} for 4 h. After natural cooling to room temperature, bright yellow g-C_3N_4 was obtained. It was ground into powder and modified by an acid treatment. The powder was dispersed in 30% aqueous HNO_3 and sonicated at 15°C for 10 h at a power of 200 W. The g-C_3N_4 nanosheets were obtained and rinsed with water.

2.4. Interfacial self-assembly of the g-C_3N_4/AuNPs nanocomposite film

The g-C_3N_4/AuNPs nanocomposite film was synthesized by two-step liquid-liquid interfacial self-assembly. The AuNPs monolayer film was fabricated by a modified oil/water/oil (O/W/O) three phase interfacial self-assembly method [25]. 125 μL of PVP-AuNPs were mixed with 2 mL of dichloromethane and 3.6 mL of H_2O were then added. The solution was stirred for 1 min to allow adequate contact between the aqueous phase and PVP-AuNPs in the oil phase. The solution was transferred to the hydrophobic PTFE sample slot and sat for 1 min. Subsequently, 2 mL of *n*-hexane were added along the wall of the container and the PVP-AuNPs were driven to the upper interface of the aqueous phase and *n*-hexane to form a closely packed PVP-AuNPs monolayer. After standing for 20 min, Si wafers were immersed in the solution and pulled out slowly to deposit and transfer the PVP-AuNPs monolayer film.

The g-C_3N_4 nanosheets were prepared by oil/water (O/W) interfacial self-assembly. 1 mL of the g-C_3N_4 nanosheets solution (0.18 mg/mL), 1 mL of H_2O, and 1 mL of *n*-hexane were mixed to form an O/W interface. 2 mL of ethanol were added dropwise to the interface to enable rapid arrangement of g-C_3N_4 at the O/W interface. After evaporation of *n*-hexane, the g-C_3N_4 film was taken out by the AuNPs monolayer film substrate to produce the g-C_3N_4/AuNPs nanocomposite film.

2.5. SERS activity

The g-C_3N_4 film, AuNPs monolayer film, and g-C_3N_4/AuNPs nanocomposite film were immersed in 1 mL of aqueous R6G aqueous solutions with different concentrations and placed in darkness overnight. Afterwards, the substrates were taken out and washed with water and dried at room temperature. The Raman scattering spectra were acquired on the Horiba Jobin-Yvon LabRam HR Vis high-resolution confocal Raman microscope with the 633 nm laser as the excitation source at room temperature. A 10 × objective lens was used, the laser power was

12 mW, and the integration time was 10 s. The Raman spectral range was 200 ~ 2000 cm^{-1}.

2.6. Photocatalytic activity

The photocatalytic activity of the g-C_3N_4 film and g-C_3N_4/AuNPs nanocomposite film was evaluated with the degradation of R6G under visible-light irradiation. The samples were immersed in 1 mL of aqueous R6G (1×10^{-5} M) and placed in darkness for 30 min to establish adsorption–desorption equilibrium. They were then irradiated by a 300 W Xenon lamp (I = 200 mW/cm^2) with a ≤400 nm cut-off filter. The solutions were subjected to absorption analysis at intervals of 5 min to determine the photocatalytic activity.

2.7. SERS monitoring of photocatalytic degradation of organic dyes

Similar to the aforementioned photocatalytic activity evaluation, the g-C_3N_4 film and g-C_3N_4/AuNPs nanocomposite film were immersed in the R6G solutions in darkness, rinsed with water, and dried at room temperature. The R6G-adsorbed of g-C_3N_4 film and g-C_3N_4/AuNPs nanocomposite film were placed in water (1 mL) and irradiated with visible light. The samples were taken out at intervals of 5 min and after washing and drying, and SERS measurements was then carried out. SERS monitoring of photocatalytic degradation of other organic dyes including methylene blue, acid orange II, and acid orange 74 was performed on g-C_3N_4/AuNPs nanocomposite film.

2.8. Characterizations

Scanning electron microscopy (SEM) and energy-dispersive X-ray spectroscopy (EDS) elemental mapping were performed on the field-emission scanning electron microscope (ZEISS SUPRA®55, Carl Zeiss, Germany). The X-ray diffraction (XRD) patterns were recorded on an X-ray diffractometer (SmartLab, Rigaku, Japan) with Cu K_α irradiation (λ = 1.5406 Å) and the absorption spectra were acquired on the ultraviolet–visible-near infrared (UV-vis-NIR) spectrophotometer (TU-1810, Puxi, China).

3. Results and discussion

3.1. Interfacial self-assembly and characterizations

The g-C_3N_4/AuNPs nanocomposite film is fabricated with a two-step interfacial self-assembly method, as illustrated in Scheme 1 [25]. Firstly, the Marangoni effect-assisted oil/water/oil (O/W/O) three-phase interfacial self-assembly process is adopted to prepare the dense and closely packed AuNPs monolayer film (Scheme 1a). Concretely, the PVP-coated AuNPs (PVP-AuNPs with a diameter of 26.2±4.7 nm) are obtained by ligand exchange with the CTAB-coated AuNPs and serve as the building blocks (Fig. S1), because the electrostatic repulsion of CTAB hinders the assembly at the O/W interface, whereas the PVP ligands facilitate the assembly [26]. The PVP-AuNPs exhibit the same LSPR peak at 534 nm as the CTAB-coated AuNPs (Fig. S1c) and the zeta potential changes from 37.40±0.62 mV to -7.18±0.49 mV (Fig. S1d), indicating the success of ligand exchange. As illustrated in Scheme 1, the ethanol solution of PVP-AuNPs is added to dichloromethane to form the oil

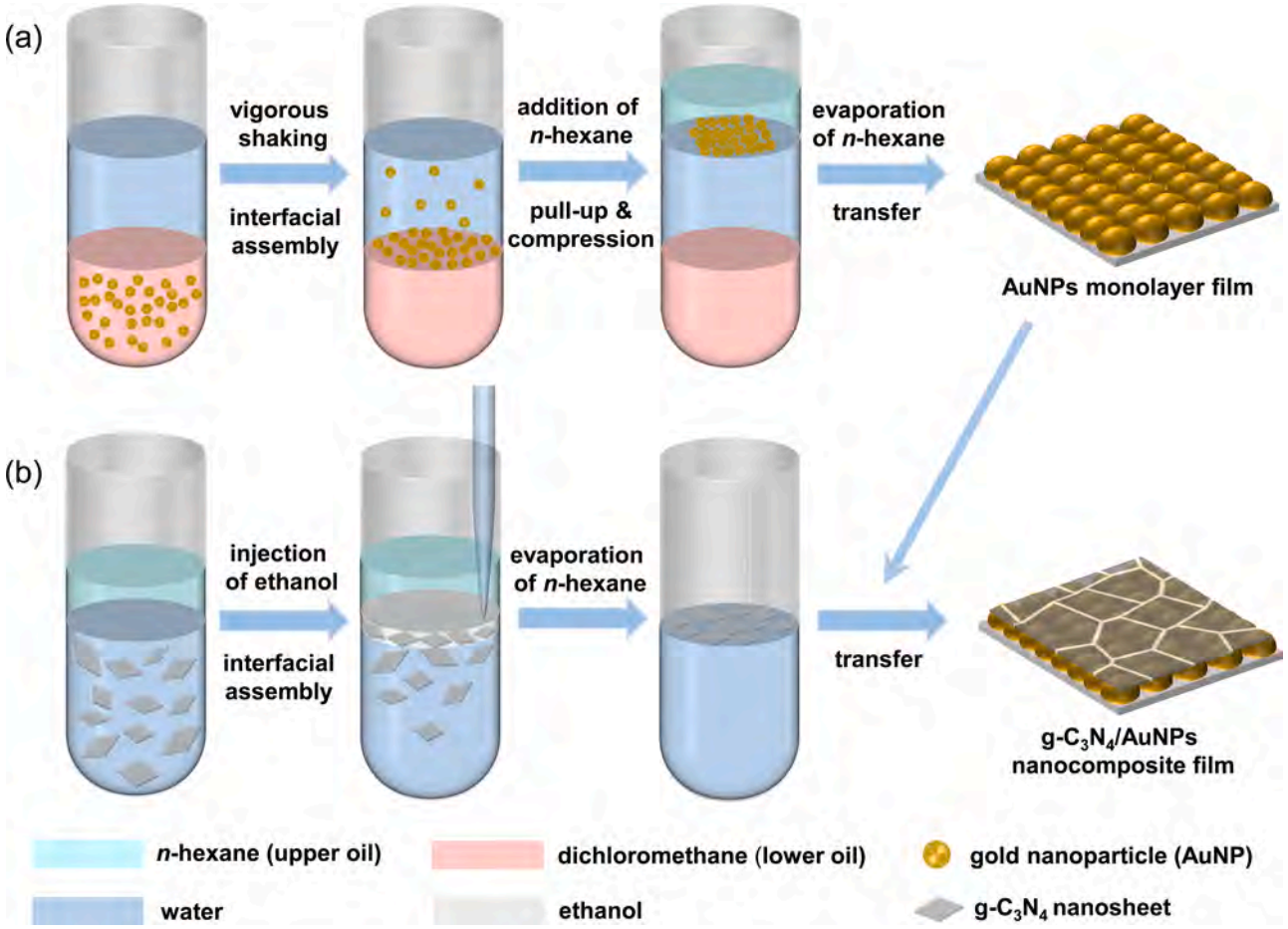

Scheme 1. Schematic illustration of the two-step liquid-liquid interface self-assembly process for the fabrication of the g-C_3N_4/AuNPs nanocomposite film.

phase and mixed with water in a hydrophobic PTFE container. After mechanical shaking, a gold film is formed at the dichloromethane/water interface (lower O/W interface) due to migration of AuNPs out of the oil phase. After introduction of *n*-hexane (another oil phase lighter than water), the gold film moves spontaneously to the *n*-hexane/water interface (upper O/W interface) so that a more closely packed AuNPs monolayer film is obtained. The Marangoni force originating from the surface tension gradient/difference between the two O/W interfaces is the main driving force for the transfer and compression of AuNPs in the three-phase assembly [27]. The surface tension of the upper *n*-hexane/water interface (γ=51.1 mN/m) is higher than that of the lower dichloromethane/water interface (γ=28.3 mN/m), and the resulting force pulls the AuNPs towards the upper O/W interface [25]. Meanwhile, the Marangoni force and lower surface potential of PVP-AuNPs help to overcome the electrostatic repulsion between AuNPs, which also contribute to the yield of the more closely packed monolayer film. The monolayer film can be transferred to a solid substrate after removal of *n*-hexane. The SEM image in Fig. 1a and cross-section SEM image in Fig. S2a confirm the close-packed AuNPs monolayer film without obvious aggregation and large voids.

The second interfacial self-assembly step is carried out with g-C_3N_4 nanosheets as the building blocks (Scheme 1b). The aqueous solution of g-C_3N_4 nanosheets and *n*-hexane are mixed to form the O/W interface. By injecting ethanol slowly, the g-C_3N_4 nanosheets move out from water and are compressed into the O/W interface due to the interfacial tension to form uniformly arranged g-C_3N_4 nanosheets. The g-C_3N_4 film is transferred to the AuNPs monolayer film after evaporation of *n*-hexane. Fig. 1b and Fig. S2c show the successful production of the g-C_3N_4/AuNPs nanocomposite film, in which g-C_3N_4 nanosheets are uniformly dispersed and supported by the ordered and closely packed AuNPs monolayer film. It is quite different from the random aggregating or dispersing of g-C_3N_4 nanosheets without assembly (Fig. S3).

The structure of the g-C_3N_4/AuNPs nanocomposite film is investigated by XRD and the XRD patterns are shown in Fig. 1c. The g-C_3N_4 film exhibits a peak at 27.65° corresponding to d-spacing of 3.34 Å for (002) for the crystal plane of g-C_3N_4 from stacking of the conjugated aromatic system [28]. The crystallized AuNPs display characteristic diffraction peaks of Au at 38.25° and 44.46° from the (111) and (200) planes of Au crystals (JCPDS No. 03-065-8601) [29]. These diffraction peaks can also be clearly observed from the pattern of g-C_3N_4/AuNPs, corroborating successful fabrication of the nanocomposite film. The EDS elemental maps (Fig. 1d) disclose uniform distributions of C, N, and Au, and the atomic concentrations of C, N and Au are determined to be 58.91%, 37.68%, and 3.41%, respectively. The g-C_3N_4/AuNPs nanocomposite film shows a broad absorption band from 500 to 1,000 nm due to LSPR of the AuNPs monolayer film [30] (Fig. 1e). More and broader absorption of visible compared to the g-C_3N_4 film bodes well for the g-C_3N_4/AuNPs nanocomposite film in the potential application in visible light absorption fields.

3.2. SERS activity and enhancement mechanism

The SERS activity of the g-C_3N_4/AuNPs nanocomposite film is investigated with the aid of the probe molecule R6G in comparison with AuNPs monolayer film and g-C_3N_4 film. Fig. 2a shows the SERS spectra of R6G at a concentration of 1×10^{-5} M for the different substrates. The SERS signals from the g-C_3N_4/AuNPs nanocomposite film is apparently the most significant. The SERS signal of R6G recorded from g-C_3N_4 film is negligible, while the R6G characteristic SERS signals are significantly amplified and can be clearly distinguished from the AuNPs monolayer film substrate. The R6G characteristic SERS signals on the AuNPs monolayer film are amplified due to LSPR-induced electromagnetic field enhancement of the periodic AuNPs arrays with nanogaps, where the strong electric field locates, as displayed in the electric field distribution analyzed by finite difference-time domain (FDTD) simulation (Fig. S4). The peaks at 612, 772, and 1126 cm^{-1} are assigned to C-C-C ring in-

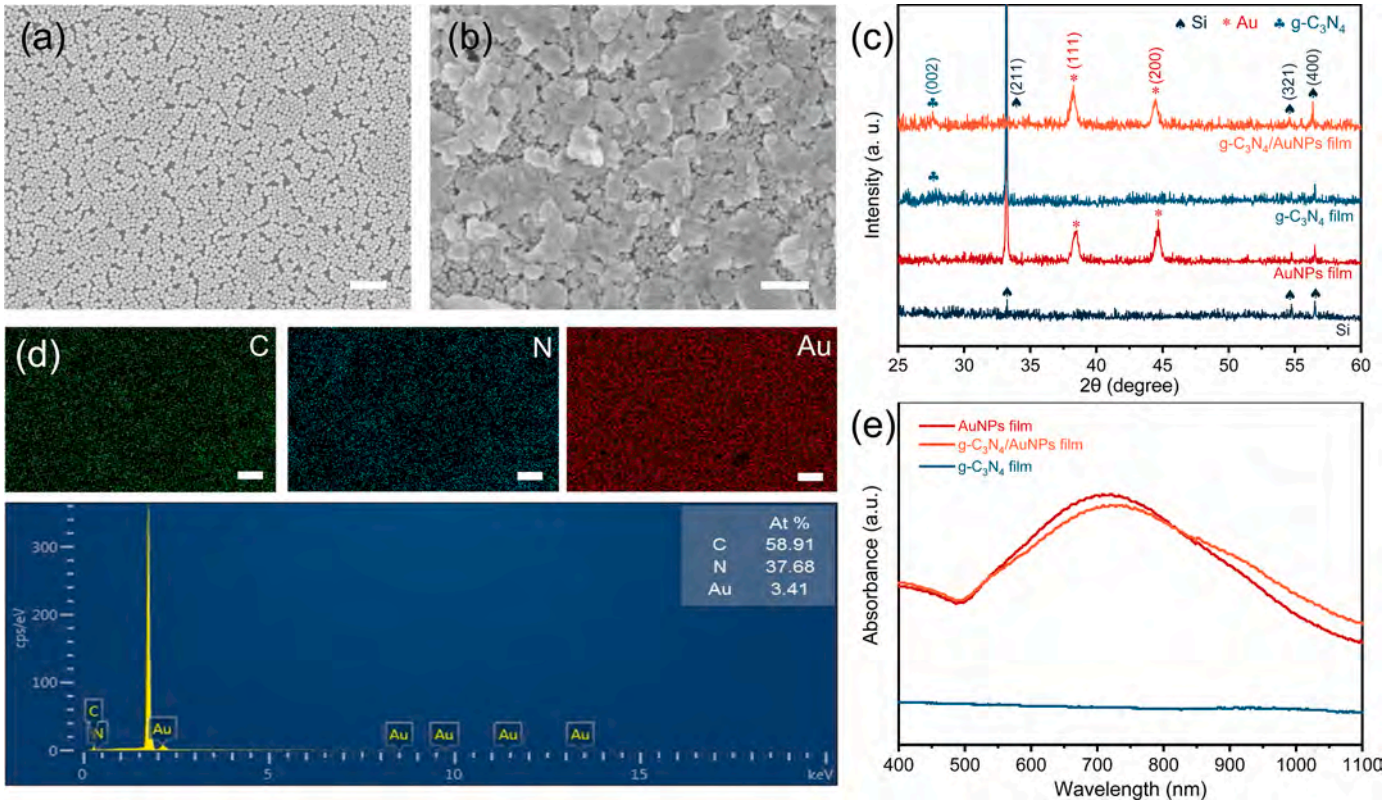

Fig. 1. (a, b) SEM images of the AuNPs monolayer film and g-C_3N_4/AuNPs nanocomposite film, respectively; (c) XRD patterns of the different films; (d) Elemental maps and EDS spectrum of the g-C_3N_4/AuNPs nanocomposite film; (e) Absorption spectra of the different films. Scale bars = 200 nm.

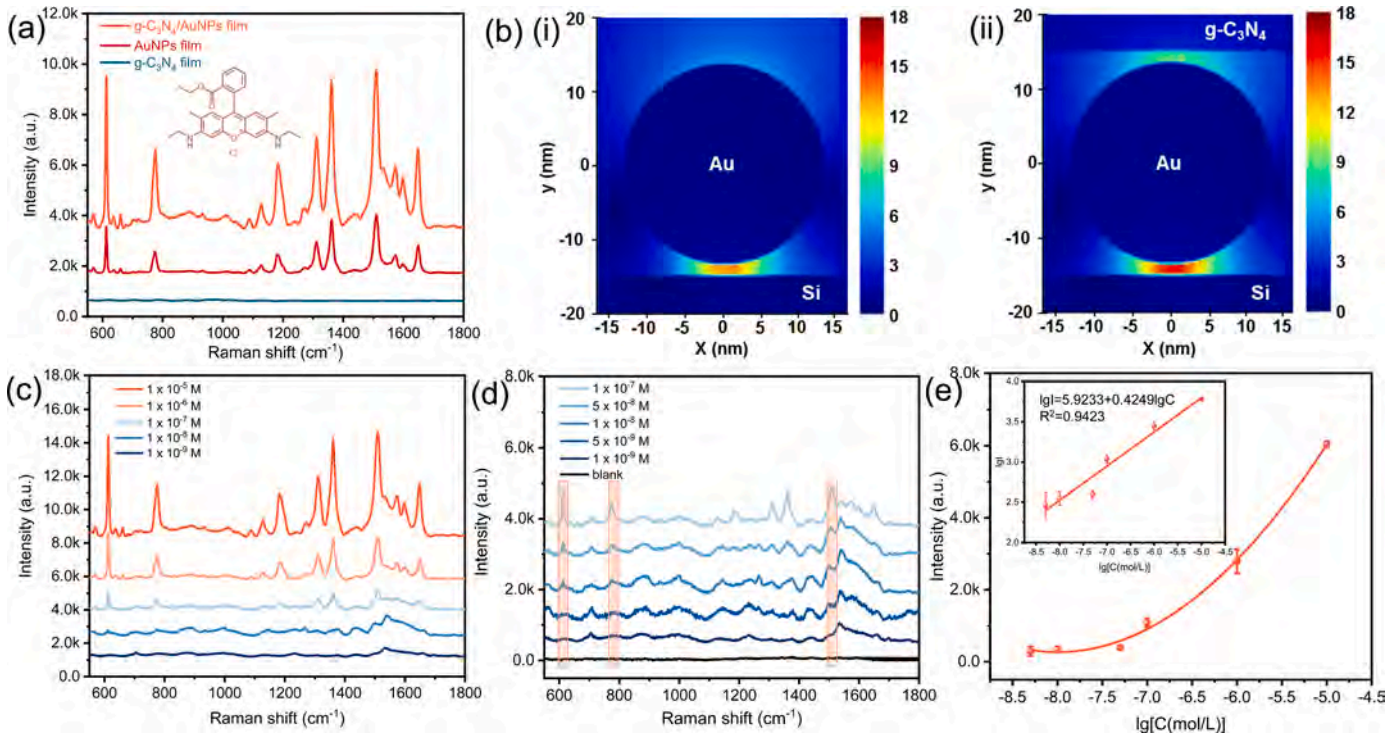

Fig. 2. (a) SERS spectra of R6G at a concentration of 1×10^{-5} M acquired from the g-C_3N_4 film, AuNPs monolayer film, and g-C_3N_4/AuNPs nanocomposite film; (b) FDTD simulation of the electromagnetic field distributions in the (i) single AuNP and (ii) g-C_3N_4 covered AuNP on Si; (c, d) Concentration-dependent SERS spectra of R6G acquired from the g-C_3N_4/AuNPs nanocomposite film for concentrations from 1×10^{-5} M to 1×10^{-9} M; (e) Intensity-concentration relationship derived from the peak at 612 cm^{-1}.

plane bending, out-of-plane bending, and C-H in-plane bending, respectively, and those at 1185, 1360, 1509, and 1649cm^{-1} correspond to in-plane C-C stretching of R6G [31]. The SERS signals of the R6G molecules on the g-C_3N_4/AuNPs nanocomposite film are stronger than those from the AuNPs monolayer film alone (Fig. 2a) due to the synergistic effects of electromagnetic enhancement and chemical enhancement. Specifically, as confirmed by FDTD simulation, besides the strong electrical fields located at the AuNPs gaps (Fig. S4), the covering of g-C_3N_4 contributes to the enhanced electric field at the g-C_3N_4/AuNPs nanogaps and AuNPs/Si nanogaps (Fig. 2b), rendering g-C_3N_4/AuNPs nanocomposite film improved electric field for the signal enhancement [32]. Meanwhile, the possible electrostatic interaction, π-π stacking and hydrogen bonding between g-C_3N_4 and R6G molecules not only lead to more adsorption of target molecules on the g-C_3N_4/AuNPs nanocomposite film, but also may contribute to possible chemical enhancement [33,34]. The enhancement factor (EF) of the g-C_3N_4/AuNPs nanocomposite film for R6G is also determined to evaluate the SERS performance [35] and the EF of the g-C_3N_4/AuNPs nanocomposite film is larger than that of the AuNPs monolayer film (1.31×10^7 *v.s.* 3.44×10^6, calculation details are provided in Supplementary Material), which confirms the more excellent SERS activity of the g-C_3N_4/AuNPs nanocomposite film.

The SERS spectra of R6G for different concentrations (1×10^{-5} to 1×10^{-9} M) acquired from the g-C_3N_4/AuNPs nanocomposite film are presented in Fig. 2c-d. The intensity drops gradually with decreasing concentration from 1×10^{-5} M to 5×10^{-9} M. The linear relationship between the intensity of the characteristic peak and concentration plotted on a logarithmic scale is generally used for quantitative analysis. As expected, the calibration curve ranged from 1×10^{-5} M to 5×10^{-9} M fitted well with the equation: lg I = 0.4249 lg C + 5.9233, with a squared correlation coefficient (R^2) of 0.9423 (Fig. 2e). The detection limit is calculated to be 8.8×10^{-10} M (S/N=3), which is comparable to the previously reported AuNPs based nanocomposite substrates in terms of detection sensitivity (Table S1). To evaluate the SERS detection uniformity, spectra are acquired from 15 random spots on the g-C_3N_4/AuNPs nanocomposite film and AuNPs monolayer film (Fig. 3a-b), and all the spectra display the quite consistent characteristic peaks of R6G. The peak at 612 cm^{-1} for R6G is monitored and relative standard deviation (RSD) is calculated [36]. As shown in Fig. 3c-d, the RSD of the AuNPs monolayer film is calculated to be 5.53%, and g-C_3N_4/AuNPs nanocomposite film also exhibits excellent reproducibility with an RSD of 9.62%. The excellent SERS activity and detection uniformity of the g-C_3N_4/AuNPs nanocomposite film suggest large potential in quantitative analysis capacity for SERS monitoring of photocatalytic reactions.

3.3. Photocatalytic degradation evaluation and mechanism

The photocatalytic degradation activity of the g-C_3N_4/AuNPs nanocomposite film is investigated by monitoring the normalized temporal concentration changes upon visible light irradiation in a short time using R6G as the organic dye model. The g-C_3N_4/AuNPs nanocomposite film is immersed in the 1×10^{-5} M R6G solution for 30 min in darkness to adsorb R6G and the concentration is determined based on the absorption peak of R6G at 526 nm. The absorption decline in Fig. S5a confirms adsorption of R6G in darkness. Afterwards, degradation of R6G is monitored at 5 min intervals based on the changes in absorption upon exposure to visible light. As shown in Fig. 4a, the absorption peak of R6G decreases gradually with irradiation time for the g-C_3N_4/AuNPs nanocomposite film. In comparison, absorption of R6G with the g-C_3N_4 film decreases more slowly within 20 min visible light irradiation (Fig. 4b). The R6G solution without visible light irradiation serves as the control and shows hardly any change (Fig. S5b). The relationship between the ln (C_t/C_0) and reaction time is obtained, where C_0 and C_t are the concentrations of R6G initially and after irradiation for time t, respectively. As shown in Fig. 4c, photocatalytic degradation on the two substrates follows the pseudo-first-order mechanism following ln (C_t/C_0) = −kt [3]. The first-order rate constant (k) of the g-C_3N_4/AuNPs nanocomposite film (0.0161 min^{-1}) is bigger than that of the g-C_3N_4 film (0.0111

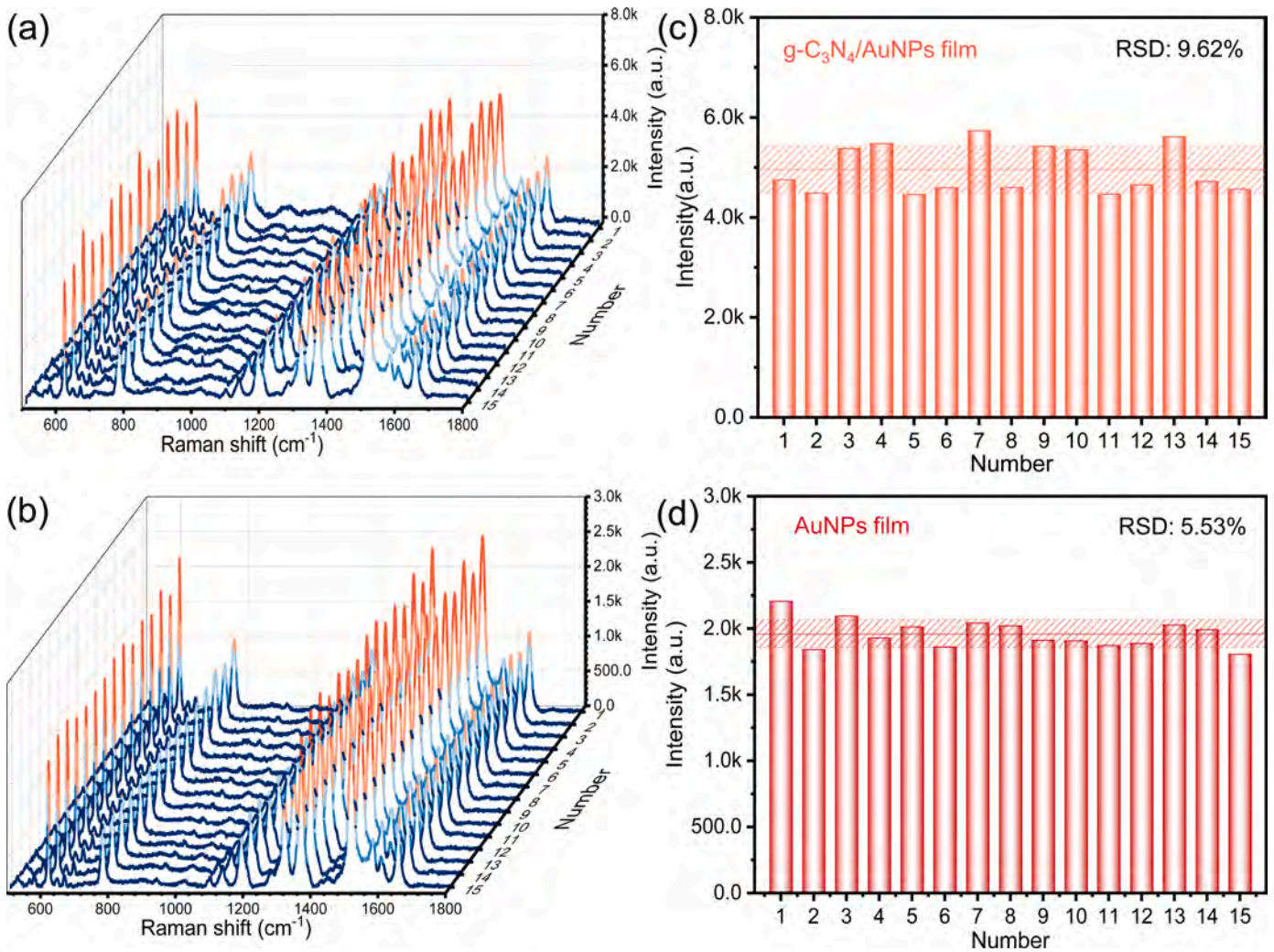

Fig. 3. (a, b) SERS spectra of R6G (1×10^{-5} M) acquired from 15 random spots on the g-C_3N_4/AuNPs nanocomposite film and AuNPs monolayer film, respectively; (c, d) Corresponding histograms of the SERS peak intensity at 612 cm^{-1} for the two substrates.

min^{-1}), indicating that g-C_3N_4/AuNPs has better performance. The enhanced photocatalytic activity can be explained with the possible mechanism illustrated in Fig. 4d. Upon irradiation by visible light, the g-C_3N_4 valence band electrons are excited to the conduction band forming electron-hole pairs, and most of the photogenerated electrons move to AuNPs [37]. The electron tapping promotes separation of the photogenerated charge carriers of g-C_3N_4, which is one of the performance enhancing features of metal-semiconductor composites photocatalysts [6]. More importantly, electrons can also be generated on the surface of AuNPs due to SPR and the SPR electric field leads to more efficient charge separation. The generated and transferred electrons reduce O_2 to $\cdot O_2^-$, and ·OH radicals can also be produced by $\cdot O_2^-$ and the holes at the valence band of g-C_3N_4 [38]. These oxidizing radial species and holes undergo the redox reactions with adsorbed R6G molecules resulting decomposition and degradation [39]. Hence, the promoted charge separation, LSPR effect, and more visible light absorption (Fig. 1e) of the nanocomposite film jointly contribute to the enhanced photocatalytic degradation activity comparing to the g-C_3N_4 film.

3.4. SERS monitoring of photocatalytic degradation of organic dyes

It is worthwhile to establish a SERS monitoring platform for the photocatalytic degradation of organic dyes, which is essential in the photocatalytic degradation studies. The photocatalytic degradation and SERS monitoring based on g-C_3N_4/AuNPs nanocomposite film is investigated with R6G. Prior to the monitoring of degradation by SERS, the influence of local heating induced by light irradiation on the nanocomposite film SERS substrate is investigated. As shown in Fig. S6, the SERS intensities of the 1×10^{-6} M R6G acquired from the substrate exhibit no significant change upon light irradiation with different time durations (0-20 min), suggesting the stable SERS activity of the nanocomposite film substrates. After adsorption of R6G molecules in darkness, visible light illumination is performed and SERS examination is carried out on the two substrates separately at 5 min intervals (Fig. 5a). Fig. 5b depicts the SERS spectra of R6G exposed to visible light irradiation for different time for the g-C_3N_4/AuNPs nanocomposite film. All the characteristic peaks of R6G are evident, whereas the SERS intensity decreases rapidly with irradiation time. This result suggests that R6G molecules are probably decomposed or degraded into CO_2, H_2O, and other small molecules that are less evident in SERS examination [33]. The SERS intensity variation of R6G observed from the AuNPs monolayer film is not significant (Fig. 5c), demonstrating poor photocatalytic activity comparatively. The control experiments without light exposure show that during the same time interval, signal decay is not obvious (Fig. S7), indicating little decomposition of R6G in darkness. The variations in the SERS intensity versus irradiation times enable analysis of the kinetics in the photocatalytic degradation process. The natural logarithm of the SERS intensities at 612 cm^{-1} are plotted versus time and the curves acquired from g-C_3N_4/AuNPs nanocomposite film and AuNPs monolayer film are displayed in Fig. 5d-e. The reactions are both found

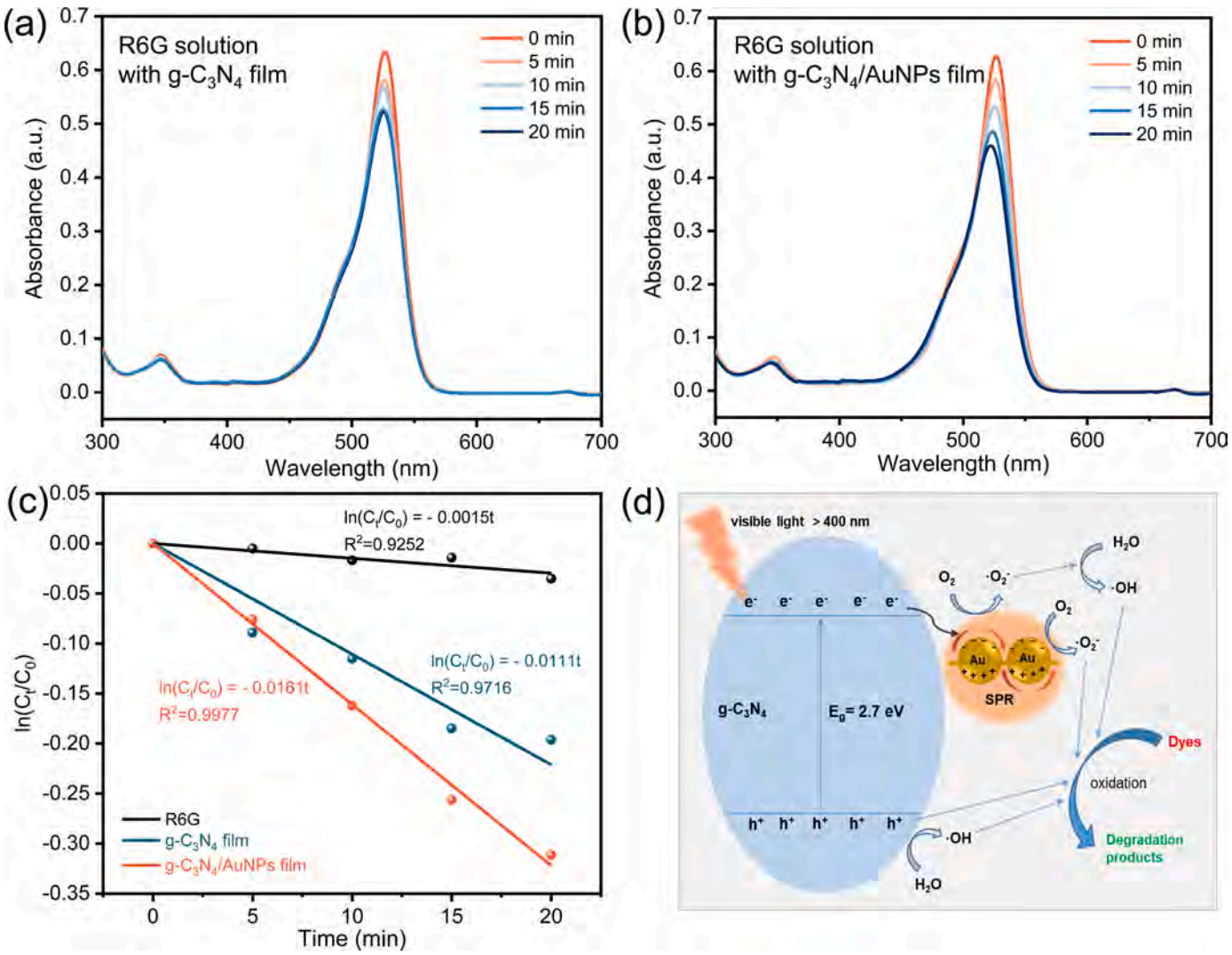

Fig. 4. (a, b) Time-dependent absorption spectra of the aqueous R6G solution within 20 min visible light irradiation for the two photocatalysts, respectively; (c) Plots of ln (C_t/C_0) versus time in the presence and absence of photocatalysts; (d) Postulated photocatalytic degradation mechanism by the g-C_3N_4/AuNPs nanocomposite film during visible light exposure.

to follow the pseudo-first-order kinetics and the curve of g-C_3N_4/AuNPs nanocomposite film shows a good linear relationship: ln (I_t/I_0) = –0.1102t (R^2 = 0.9939), while that from AuNPs monolayer shows the following relationship: ln (I_t/I_0) = –0.0479t (R^2 = 0.9658). The plots of ln (I_t/I_0) versus time for the peaks at 772, 1126, 1185, 1360, 1509, and 1649cm^{-1} during photocatalytic degradation on g-C_3N_4/AuNPs nanocomposite film are also drawn in Fig. S8, and results show that the characteristic bonds of R6G degrade at the similar reaction rate. The high reaction rate photocatalytic degradation of organic dyes and the reaction kinetics analysis are successfully achieved on g-C_3N_4/AuNPs nanocomposite film.

The g-C_3N_4/AuNPs nanocomposite film is further applied to the photocatalytic degradation and reaction monitoring of other organic dyes including methylene blue, acid orange II, and acid orange 74. The g-C_3N_4/AuNPs nanocomposite films are immersed separately in the dye solutions (1×10^{-5} M methylene blue, 1×10^{-3} M acid orange II, and 1×10^{-3} M acid orange 74), sat in darkness, and then exposed to visible light similar to the protocols for R6G. The SERS spectral features of methylene blue, orange II, and acid orange 74 after photocatalytic degradation for different time by g-C_3N_4/AuNPs nanocomposite film are presented in Fig. 6a-c, respectively. The major characteristic bands of methylene blue (466, 499, 710, 1152, 1395 and 1623 cm^{-1}), acid orange II (1230, 1496, and 1594 cm^{-1}), and acid orange 74 (520, 783, 1037 and 1386 cm^{-1}) are observed and the detailed assignments are listed in Table S2. The peak intensities diminish with irradiation time indicating degradation proceeds with light irradiation. The relationships between the SERS intensities and irradiation time for the three dyes are presented in Fig. 6d-f, respectively. Similar to the SERS monitoring of photocatalytic degradation of R6G, the degradation kinetics of methylene blue, acid orange II, and acid orange 74 also follow the pseudo-first-order mechanism: ln (I_t/I_0) = −0.1630t, ln (I_t/I_0) = −0.0893t, and ln (I_t/I_0) = −0.0826t for methylene blue, acid orange II, and acid orange 74, respectively. These results suggest the good capability of g-C_3N_4/AuNPs nanocomposite film in the detection and monitoring of photocatalytic degradation of different organic dyes.

4. Conclusions

The g-C_3N_4/AuNPs nanocomposite film consisting of orderly arranged g-C_3N_4 film anchored on the closely packed AuNPs monolayer film is designed and fabricated by two-step interfacial assembly, and is developed as dual-functional nanoplatform for photocatalytic degradation of organic dyes and SERS monitoring of degradation reactions. The nanocomposite film delivers excellent SERS performance with excellent detection sensitivity and uniformity. The g-C_3N_4/AuNPs film has excellent visible-light photocatalytic degradation capability for different

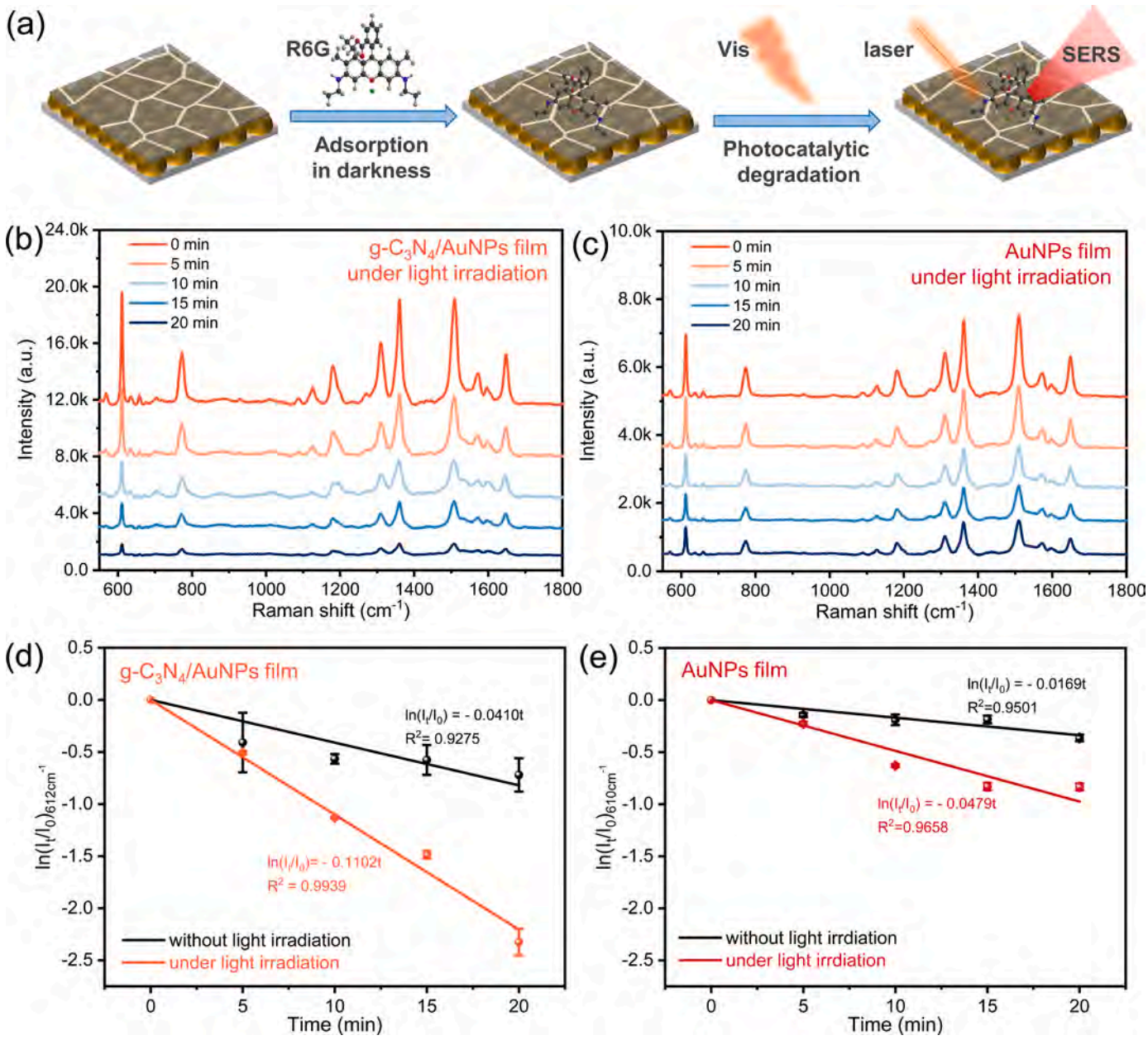

Fig. 5. (a) Schematic illustration of the SERS monitoring process of photocatalytic degradation of organic dyes; (b, c) SERS spectra recorded at 5 min intervals during photocatalytic degradation of 1×10^{-5} M R6G on the g-C_3N_4/AuNPs nanocomposite film and AuNPs monolayer film, respectively; (d, e) Plots of ln (I_t/I_0) versus time for the peak at 612 cm^{-1} with or without light irradiation.

organic dye molecules including R6G, methylene blue, acid orange II, and acid orange 74, while the reaction kinetics can be studied by SERS monitoring at the same time. The photocatalytic degradation mechanisms are proposed and determined. The results show that g-C_3N_4/AuNPs nanocomposite film has large potential in visible-light photocatalytic degradation of organic dye pollutants besides reaction monitoring by means of SERS.

Data availability

Data will be made available on request.

Supplementary materials

Supplementary data associated with this article can be found in the online version.

CRediT authorship contribution statement

Wanling Chen: Methodology, Investigation, Data curation. **Wanlin Wang:** Methodology, Investigation. **Hongyun Xing:** Methodology, Investigation. **Wan Li:** Data curation. **Haiwei He:** Methodology, Investigation. **Wei Li:** Data curation. **Paul K. Chu:** Funding acquisition, Writing – review & editing. **Guofen Song:** Data curation, Funding acquisition. **Huaiyu Wang:** Funding acquisition, Writing – review & editing. **Penghui Li:** Conceptualization, Data curation, Funding acquisition, Writing – original draft, Writing – review & editing, Supervision.

Declaration of Competing Interest

The authors declare that they have no known competing financial interests or personal relationships that could have appeared to influence the work reported in this paper.

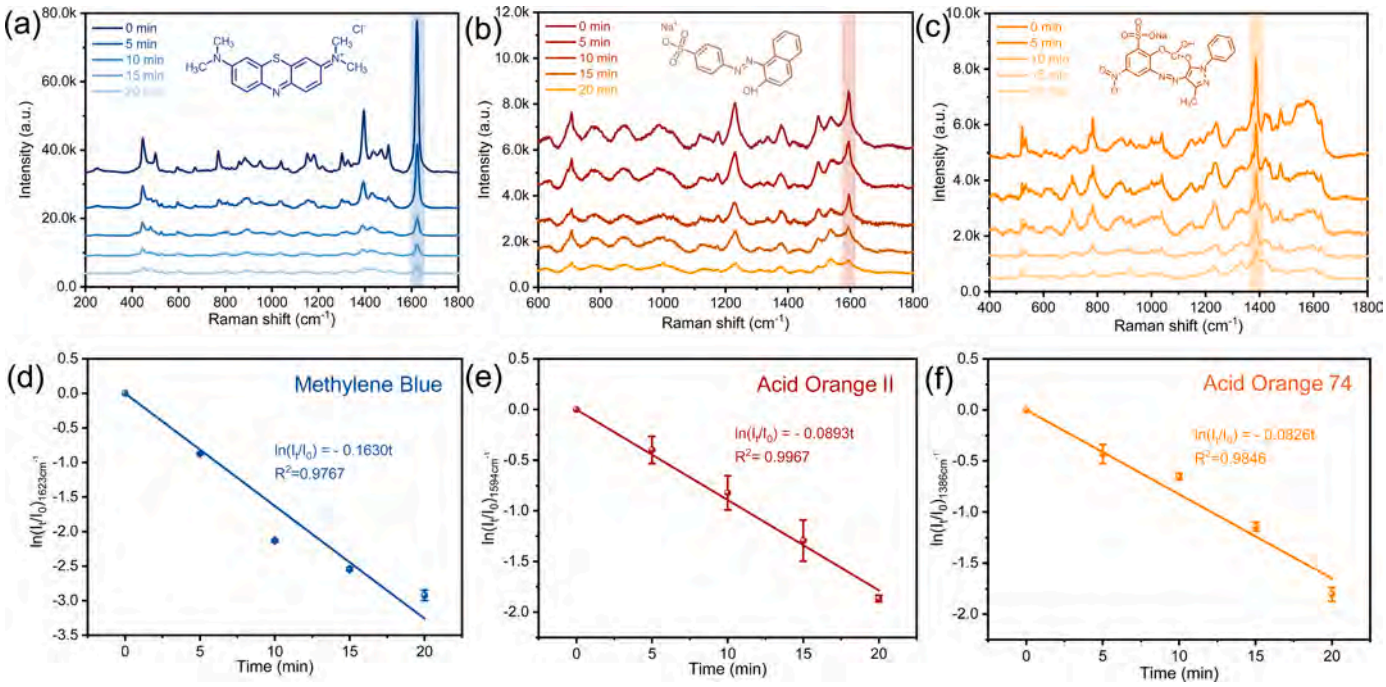

Fig. 6. (a, b, c) SERS spectra recorded at 5 min intervals during photocatalytic degradation on the g-C_3N_4/AuNPs nanocomposite film of 1×10^{-5} M methylene blue, 1×10^{-3} M acid orange II, and 1×10^{-3} M acid orange 74, respectively; (d, e, f) Plots of ln (I_t/I_0) versus time for the characteristic peak of the g-C_3N_4/AuNPs nanocomposite film for methylene blue (1623 cm^{-1}), acid orange II (1594 cm^{-1}), and acid orange 74 (1386 cm^{-1}), respectively. (For interpretation of the references to colour in this figure legend, the reader is referred to the web version of this article.).

Data availability

Data will be made available on request.

Acknowledgements

This work was financially supported by National Key R&D Program of China (No. 2020YFA0908800), National Natural Science Foundation of China (Nos. 32000981, 31922040 and 81903057), Guangdong Basic and Applied Basic Research Foundation (No. 2019A1515111209), Shenzhen Science and Technology Program (Nos. JCYJ20210324102202007 and JCYJ20190806170011328), Science and Technology Innovation Project of Foshan City (No. 1920001000025), as well as City University of Hong Kong Donation Research Grant (No. DON-RMG 9229021).

Supplementary materials

Supplementary material associated with this article can be found, in the online version, at doi:10.1016/j.surfin.2023.102808.

References

[1] Y. He, X. Fu, B. Li, H. Zhao, D. Yuan, B. Na, Highly efficient organic dyes capture using thiol-functionalized porous organic polymer, ACS Omega 7 (2022) 17941–17947.
[2] S. Li, W. Liu, S. Zhao, Y. Li, K. Chen, Enhanced photocatalytic performance of NiS_2/g-C_3N_4/SnS_2 by improving the charge diffusion on both valence band and conduction band of carbon nitride, ChemistrySelect 6 (2021) 4440–4447.
[3] Q. Chen, W. Liang, X. Shi, M. Yang, X. Qin, L. Jiang, C. Jia, F. Chen, D. Luo, Photodegradation and in-situ SERS monitoring properties of Ag@AgCl anchored on sea urchin-shaped Fe_3O_4@C/1D PANI nanoparticles, ChemistrySelect 7 (2022), e202104495.
[4] P. Shoghi, M. Hamzehloo, Facile fabrication of novel Z-scheme g-C_3N_4 nanosheets/$Bi_7O_9I_3$ photocatalysts with highly rapid photodegradation of RhB under visible light irradiation, J. Colloid Interf. Sci. 616 (2022) 453–464.
[5] Y. He, J. Huang, B. Wang, Y. Qu, Construction of Z-scheme heterojunction C_3N_4/N-CQDs@$W_{18}O_{49}$ for full-spectrum photocatalytic organic pollutant degradation, Appl. Surf. Sci. 610 (2022), 155255.
[6] J. Fu, J. Yu, C. Jiang, B. Cheng, g-C_3N_4-based heterostructured photocatalysts, Adv. Energy Mater. 8 (2018), 1701503.
[7] C.L. Warkentin, Z. Yu, A. Sarkar, R.R. Frontiera, Decoding chemical and physical processes driving plasmonic photocatalysis using surface-enhanced Raman spectroscopies, Acc. Chem. Res. 54 (2021) 2457–2466.
[8] J. Huang, Y. Zhu, M. Lin, Q. Wang, L. Zhao, Y. Yang, K.X. Yao, Y. Han, Site-Specific Growth of Au−Pd Alloy Horns on Au Nanorods: A platform for highly sensitive monitoring of catalytic reactions by surface enhancement Raman spectroscopy, J. Am. Chem. Soc. 135 (2013) 8552–8561.
[9] Y. Li, Y. Hu, F. Shi, H. Li, W. Xie, J. Chen, C-H arylation on nickel nanoparticles monitored by in situ surface-enhanced Raman spectroscopy, Angew. Chem. Int. Ed. 58 (2019) 9049–9053.
[10] L. Qiu, G.A. Pang, G. Zheng, D. Bauer, K. Wieland, C. Haisch, Kinetic and mechanistic investigation of the photocatalyzed surface reduction of 4-nitrothiophenol observed on a silver plasmonic film via surface-enhanced Raman scattering, ACS Appl. Mater. Interfaces 12 (2020) 21133–21142.
[11] J.-H. Zhong, X. Jin, L. Meng, X. Wang, H.-S. Su, Z.-L. Yang, C.T. Williams, B. Ren, Probing the electronic and catalytic properties of a bimetallic surface with 3nm resolution, Nat. Nanotechnol. 12 (2017) 132–136.
[12] H. Zhang, C. Wang, H.-L. Sun, G. Fu, S. Chen, Y.-J. Zhang, B.-H. Chen, J.R. Anema, Z.-L. Yang, J.-F. Li, Z.-Q. Tian, In situ dynamic tracking of heterogeneous nanocatalytic processes by shell-isolated nanoparticle-enhanced Raman spectroscopy, Nat. Commun. 8 (2017) 15447.
[13] H.-S. Su, H.-S. Feng, Q.-Q. Zhao, X.-G. Zhang, J.-J. Sun, Y. He, S.-C. Huang, T.-X. Huang, J.-H. Zhong, D.-Y. Wu, B. Ren, Probing the local generation and diffusion of active oxygen species on a Pd/Au bimetallic surface by tip-enhanced Raman spectroscopy, J. Am. Chem. Soc. 142 (2020) 1341–1347.
[14] J.-C. Dong, X.-G. Zhang, V. Briega-Martos, X. Jin, J. Yang, S. Chen, Z.-L. Yang, D.-Y. Wu, J.M. Feliu, C.T. Williams, Z.-Q. Tian, J.-F. Li, In situ Raman spectroscopic evidence for oxygen reduction reaction intermediates at platinum single-crystal surfaces, Nat. Energy 4 (2019) 60–67.
[15] L. Yuan, Z. Geng, J. Xu, F. Guo, C. Han, Metal-Semiconductor heterostructures for photoredox catalysis: Where are we now and where do we go? Adv. Funct. Mater. 31 (2021), 2101103.
[16] D. Liu, C. Xue, Plasmonic coupling architectures for enhanced photocatalysis, Adv. Mater. 33 (2021), 2005738.
[17] S. Almohammed, S.T. Barwich, A.K. Mitchell, B.J. Rodriguez, J.H. Rice, Enhanced photocatalysis and biomolecular sensing with field-activated nanotube-nanoparticle templates, Nat. Commun. 10 (2019) 2496.
[18] S. Cong, X. Liu, Y. Jiang, W. Zhang, Z. Zhao, Surface enhanced Raman scattering revealed by interfacial charge-transfer transitions, The Innovation 1 (2020), 100051.

[19] S. Cong, Z. Wang, W. Gong, Z. Chen, W. Lu, J.R. Lombardi, Z. Zhao, Electrochromic semiconductors as colorimetric SERS substrates with high reproducibility and renewability, Nat. Commun. 10 (2019) 678.
[20] L. Xing, Y. Xiahou, X. Zhang, W. Du, P. Zhang, H. Xia, Large-area monolayer films of hexagonal close-packed Au@Ag nanoparticles as substrates for SERS-based quantitative determination, ACS Appl. Mater. Interfaces 14 (2022) 13480–13489.
[21] C. Song, B. Ye, J. Xu, J. Chen, W. Shi, C. Yu, C. An, J. Zhu, W. Zhang, Large-area nanosphere self-assembly monolayers for periodic surface nanostructures with ultrasensitive and spatially uniform SERS sensing, Small 18 (2021), 2104202.
[22] P. Li, Y. Li, Z.-K. Zhou, S. Tang, X.-F. Yu, S. Xiao, Z. Wu, Q. Xiao, Y. Zhao, H. Wang, P.K. Chu, Evaporative self-assembly of gold nanorods into macroscopic 3D plasmonic superlattice arrays, Adv. Mater. 28 (2016) 2511–2517.
[23] S. Tang, Y. Li, H. Huang, P. Li, Z. Guo, Q. Luo, Z. Wang, P.K. Chu, J. Li, X.-F. Yu, Efficient enrichment and self-assembly of hybrid nanoparticles into removable and magnetic SERS substrates for sensitive detection of environmental pollutants, ACS Appl. Mater. Interfaces 9 (2017) 7472–7480.
[24] A. Abdullah, M. Altaf, H.I. Khan, G.A. Khan, W. Khan, A. Ali, A.S. Bhatti, S.U. Khan, W. Ahmed, Facile room temperature synthesis of multifunctional CTAB coated gold nanoparticles, Chem. Phys. 510 (2018) 30–36.
[25] X. Lin, G. Fang, Y. Liu, Y. He, L. Wang, B. Dong, Marangoni effect-driven transfer and compression at three-phase interfaces for highly reproducible nanoparticle monolayers, J. Phys. Chem. Lett. 11 (2020) 3573–3581.
[26] L. Tian, M. Su, F. Yu, Y. Xu, X. Li, L. Li, H. Liu, W. Tan, Liquid-state quantitative SERS analyzer on self-ordered metal liquid-like plasmonic arrays, Nat. Commun. 9 (2018) 3642.
[27] J. Wang, C. Teng, Y. Jiang, Y. Zhu, L. Jiang, Wetting-induced climbing for transferring interfacially assembled large-area ultrathin pristine graphene film, Adv. Mater. 31 (2019), 1806742.
[28] Y. Yu, D. Chen, W. Xu, J. Fang, J. Sun, Z. Liu, Y. Chen, Y. Liang, Z. Fang, Synergistic adsorption-photocatalytic degradation of different antibiotics in seawater by a porous g-C_3N_4/calcined-LDH and its application in synthetic mariculture wastewater, J. Hazard. Mater. 416 (2021), 126183.
[29] Y. Guo, S. Zhu, H. Bao, H. Fu, H. Zhang, L. Zhou, Y. Li, W. Cai, Abnormally weak surface-enhanced Raman scattering activity of tip-rich Au nanostars: The role of interfacial defects, J. Phys. Chem. Lett. 13 (2022) 2428–2433.
[30] X. Li, H. Liu, Y. Chen, C. Gu, G. Wei, J. Zhou, T. Jiang, Construction of reusable PMMA−Ag/g-C_3N_4/Ag hybrid substrates with plasmonic-enhanced intrinsic Raman signals for quantitative SERS detection and green degradation, ACS Sustainable Chem. Eng. 9 (2021) 12885–12898.
[31] X. Chong, B. Zhao, R. Li, W. Ruan, X. Yang, Photocatalytic degradation of rhodamine6G on Ag modified TiO_2 nanotubes: Surface enhanced Raman scattering study on catalytic kinetics and substrate recyclability, Colloids and Surfaces A: Physicochem. Eng. Aspects 481 (2015) 7–12.
[32] Y. Ma, L. Yang, Y. Yang, Y. Peng, Y. Wei, Z. Huang, Multifunctional Ag-decorated g-C_3N_4 nanosheets as recyclable SERS substrates for CV and RhB detection, RSC Adv 8 (2018) 22095–22102.
[33] L.-L. Qu, Z.-Q. Geng, W. Wang, K.-C. Yang, W.-P. Wang, C.-Q. Han, G.-H. Yang, R. Vajtai, D.-W. Li, P.M. Ajayan, Recyclable three-dimensional Ag nanorod arrays decorated with O-g-C_3N_4 for highly sensitive SERS sensing of organic pollutants, J. Hazard. Mater. 379 (2019), 120823.
[34] Y.-N. Wang, Y. Zhang, W.-S. Zhang, Z.-R. Xu, A SERS substrate of mesoporous g-C_3N_4 embedded with in situ grown gold nanoparticles for sensitive detection of 6-thioguanine, Sens. Actuators B-Chem. 260 (2018) 400–407.
[35] H. Lai, H. Dai, G. Li, Z. Zhang, Rapid determination of pesticide residues in fruit and vegetable using Au@AgNPs decorated 2D Ni-MOF nanosheets as efficient surface-enhanced Raman scattering substrate, Sens. Actuators B-Chem. 369 (2022), 132360.
[36] H. Xie, P. Li, J. Shao, H. Huang, Y. Chen, Z. Jiang, P.K. Chu, X.-F. Yu, Electrostatic self-assembly of Ti_3C_2Tx MXene and gold nanorods as an efficient surface-enhanced Raman scattering platform for reliable and high-sensitivity determination of organic pollutants, ACS Sens 4 (2019) 2303–2310.
[37] M. Wang, M. Ye, J. Iocozzia, C. Lin, Z. Lin, Plasmon-mediated solar energy conversion via photocatalysis in noble metal/semiconductor composites, Adv. Sci. 3 (2016), 1600024.
[38] A. Mohammad, M.R. Karim, M.E. Khan, M.M. Khan, M.H. Cho, Biofilm-assisted fabrication of Ag@SnO_2-g-C_3N_4 nanostructures for visible light-induced photocatalysis and photoelectrochemical performance, J. Phys. Chem. C 123 (2019) 20936–20948.
[39] L. Zhao, C. Deng, S. Xue, H. Liu, L. Hao, M. Zhu, Multifunctional g-C_3N_4/Ag NPs intercalated GO composite membrane for SERS detection and photocatalytic degradation of paraoxon-ethyl, Chem. Eng. J. 402 (2020), 126223.

Supplementary Material

Interfacial self-assembled dual-functional nanocomposite films for SERS monitoring of visible-light photocatalytic degradation of organic dye pollutants

Wanling Chen[a], Wanlin Wang[b], Hongyun Xing[b], Wan Li[a], Haiwei He[a, c], Wei Li[a], Paul K. Chu[d], Guofen Song[a,*], Huaiyu Wang[a, c, *], Penghui Li[a, c, *]

[a] *Institute of Biomedicine and Biotechnology, Shenzhen Institute of Advanced Technology, Chinese Academy of Sciences, Shenzhen 518055, China*

[b] *College of Electronics and Information Engineering, Shenzhen University, Shenzhen, 518060, China*

[c] *University of Chinese Academy of Sciences, Beijing 100049, China*

[d] *Department of Physics, Department of Materials Science and Engineering, and Department of Biomedical Engineering, City University of Hong Kong, Tat Chee Avenue, Kowloon, Hong Kong, China*

* Corresponding authors.

Email addresses: gf.song@siat.ac.cn (G. Song), hy.wang1@siat.ac.cn (H. Wang), ph.li@siat.ac.cn (P. Li).

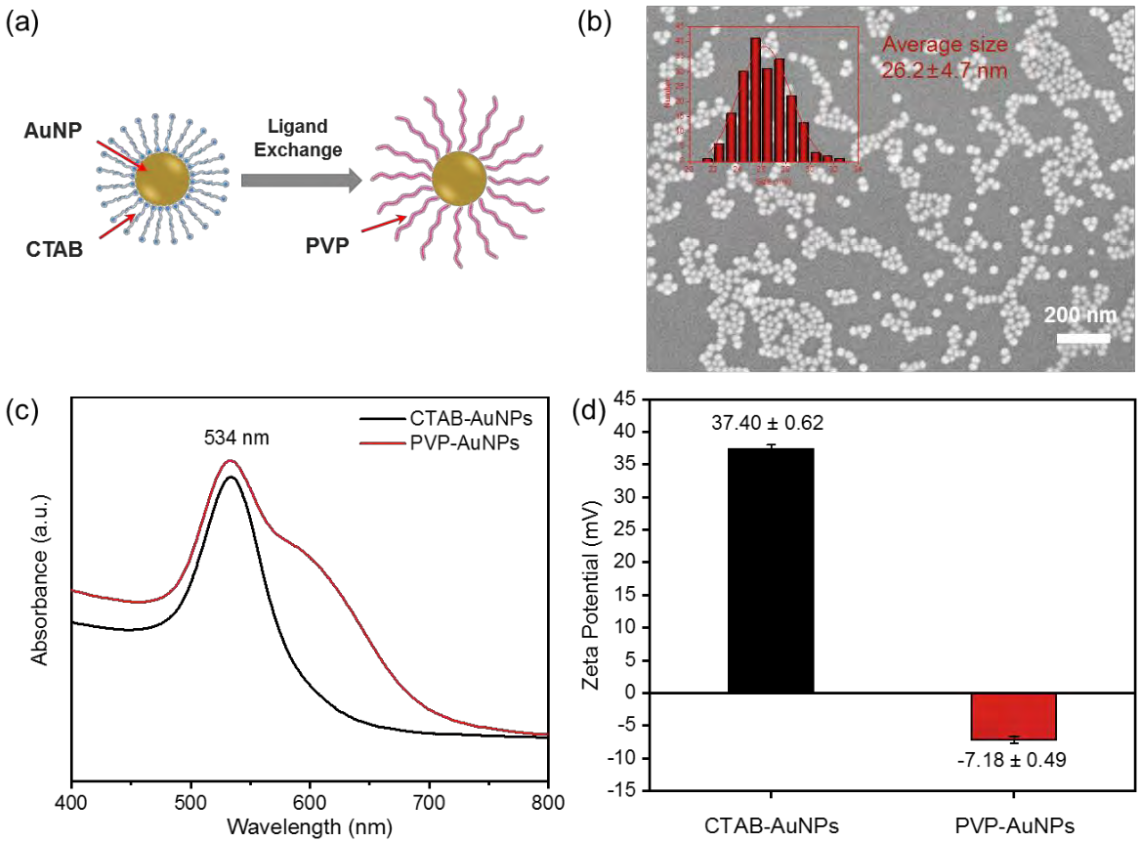

Fig. S1. (a) Schematic illustration for the preparation of PVP-AuNPs by surface ligand exchange; (b) SEM image of PVP-AuNPs with the inset showing the size distribution acquired by Image J; (c) UV-vis spectra of CTAB-AuNPs and PVP-AuNPs; (d) Zeta potential changes of AuNPs after ligand exchange.

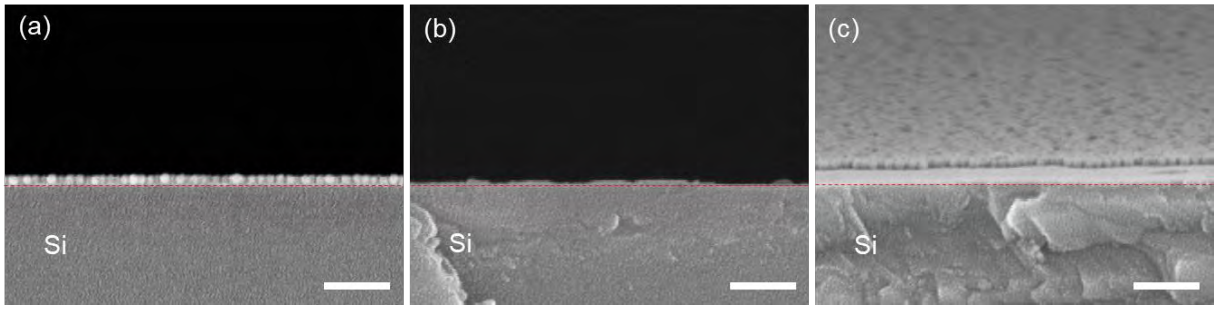

Fig. S2. (a-c) Cross-section SEM images of AuNPs monolayer film, g-C_3N_4 nanosheets layer, and g-C_3N_4/AuNPs nanocomposite film on Si substrates, respectively. Scale bars = 200 nm.

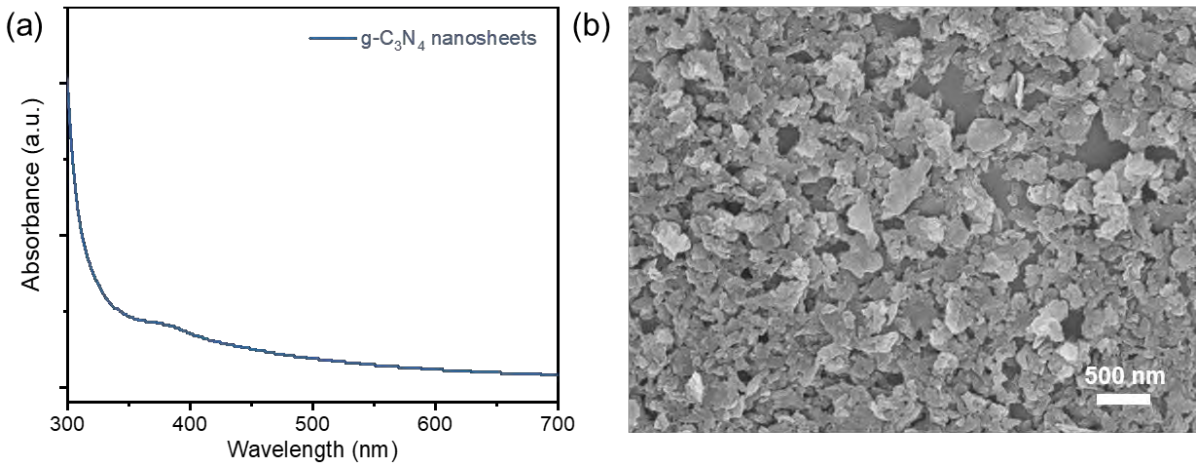

Fig. S3. (a) UV-vis spectrum of the g-C_3N_4 nanosheets aqueous suspension and (b) SEM image of g-C_3N_4 nanosheets.

Finite difference-time domain (FDTD) modeling

For the FDTD simulations, a model consisting of g-C_3N_4/AuNPs nanocomposite on Si is established using a FDTD program. The mesh size is chosen to achieve a balance between the required computer memory and the simulation time while ensuring convergence of the results. The diameter of AuNPs is set to 26.5 nm and their gap is set to 1.5 nm. The thickness of g-C_3N_4 is 10 nm and the refractive index of g-C_3N_4 is estimated to be 1.65 [1]. A plane-wave source with a wavelength of 633 nm illuminates the substrates vertically from the (100) and (010) direction considering scattering in actual situation. The boundary condition (010) direction is set to provide a perfectly matched layer, and the boundary condition in (100) direction is set to be periodic boundary.

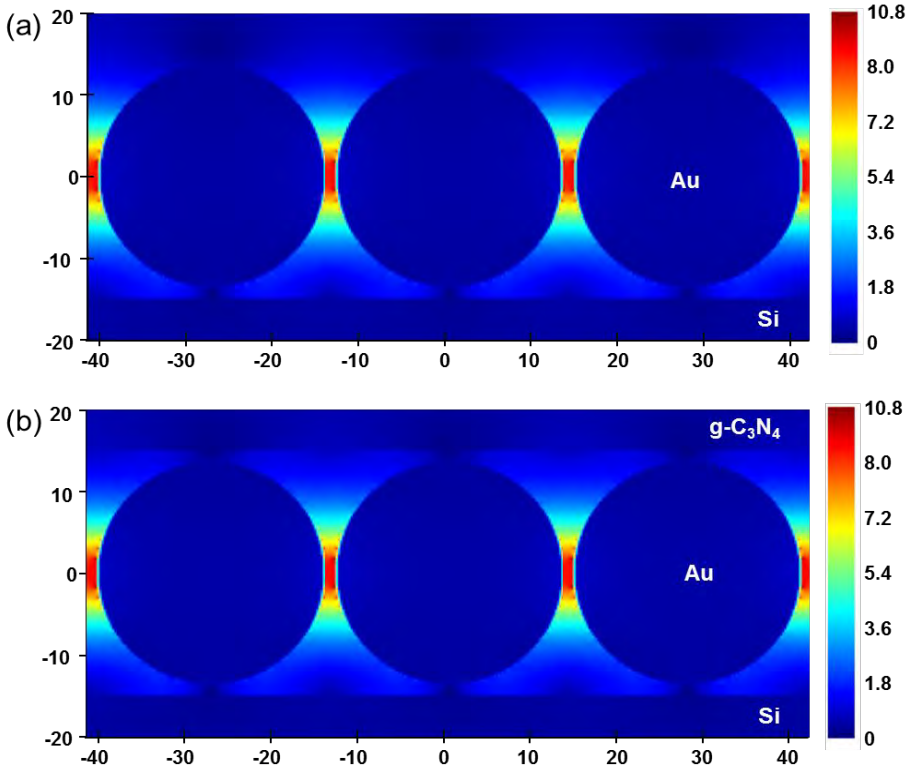

Fig. S4. (a, b) FDTD simulation of the electromagnetic field distributions of the periodic AuNPs array without and with covering g-C_3N_4 nanosheets.

Calculation of Enhancement Factor

The enhancement factor (EF) of the substrates for R6G is estimated according to the following equation [2]:

$$EF = (I_{SERS}/I_{Raman}) \times (C_{Raman}/C_{SERS}),$$

where I_{SERS} is the SERS intensity of R6G with a concentration of C_{SERS} obtained on SERS substrate and I_{Raman} is the normal Raman intensity of R6G with a concentration of C_{Raman} obtained on silicon. For the g-C_3N_4/AuNPs nanocomposite film substrate, I_{SERS} of 612 cm^{-1} for C_{SERS} of 5×10^{-9} M is 291.88 counts. I_{Raman} for C_{Raman} of 0.1 M obtained on silicon is 446.69 counts and EF is calculated to be 1.31×10^{7}. For the AuNPs monolayer film substrate, I_{SERS} of 612 cm^{-1} for C_{SERS} of 5×10^{-9} M is 76.74 counts. I_{Raman} for C_{Raman} of 0.1 M obtained on silicon is 446.69 counts and EF is calculated to be 3.44×10^{6}.

Table S1. Comparison of the SERS performance in terms of limit of detection towards R6G with AuNPs based nanocomposites.

Substrate	**Detection limit**	**Ref.**
gold nanoparticles/reduced graphene oxide	5×10^{-7} M	[3]
Au-decorated cellulose	1×10^{-9} M	[4]
CVD graphene- AuNPs	8×10^{-7} M	[5]
graphene-Au nanosphere	1×10^{-6} M	[6]
Au nanoparticles/graphene oxide/cicada wing	1×10^{-8} M	[7]
g-C_3N_4/AuNPs nanocomposite films	8.8×10^{-10} M	this work

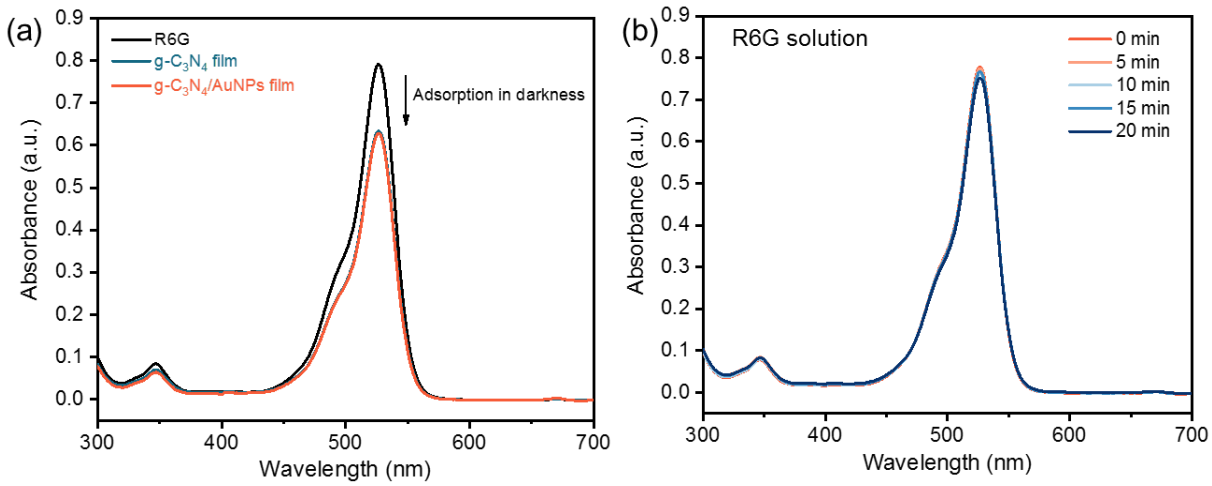

Fig. S5. (a) Absorption spectra of the R6G aqueous solution before and after adsorption for the g-C_3N_4/AuNPs nanocomposite film and g-C_3N_4 film in darkness; (b) Time-dependent absorption spectra of the R6G aqueous solution without visible light irradiation and photocatalysts.

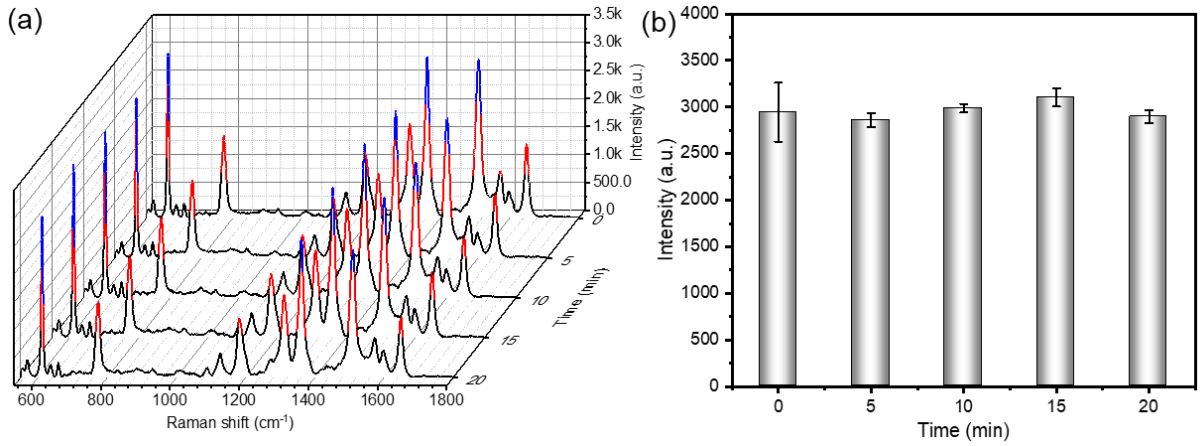

Fig. S6. (a) SERS spectra of 1×10^{-6} M R6G recorded on the g-C_3N_4/AuNPs nanocomposite film substrates subjected to different periods of light irradiation, and (b) corresponding intensities of the peaks at 612 cm^{-1}.

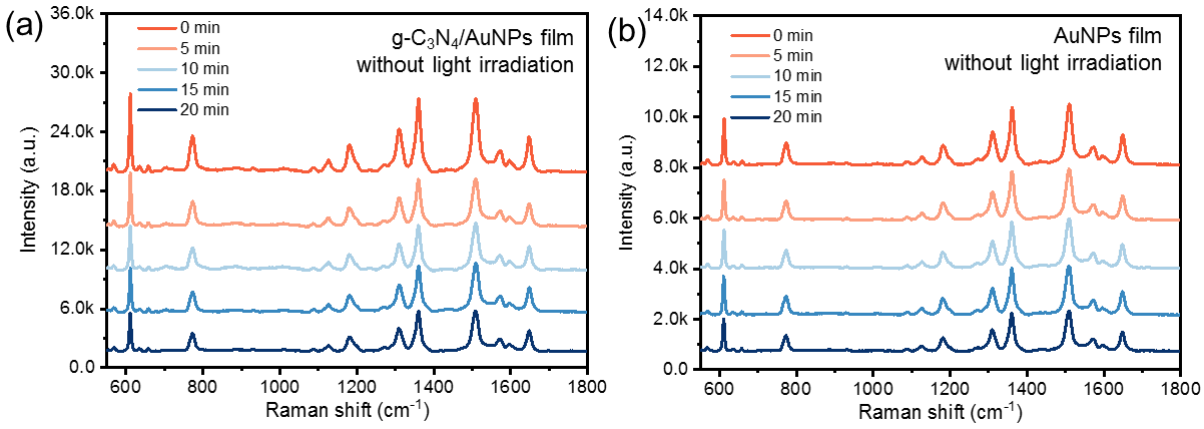

Fig. S7. SERS spectra of 1×10^{-5} M R6G recorded at 5 min intervals without light irradiation on (a) g-C_3N_4/AuNPs nanocomposite film and (b) AuNPs monolayer film.

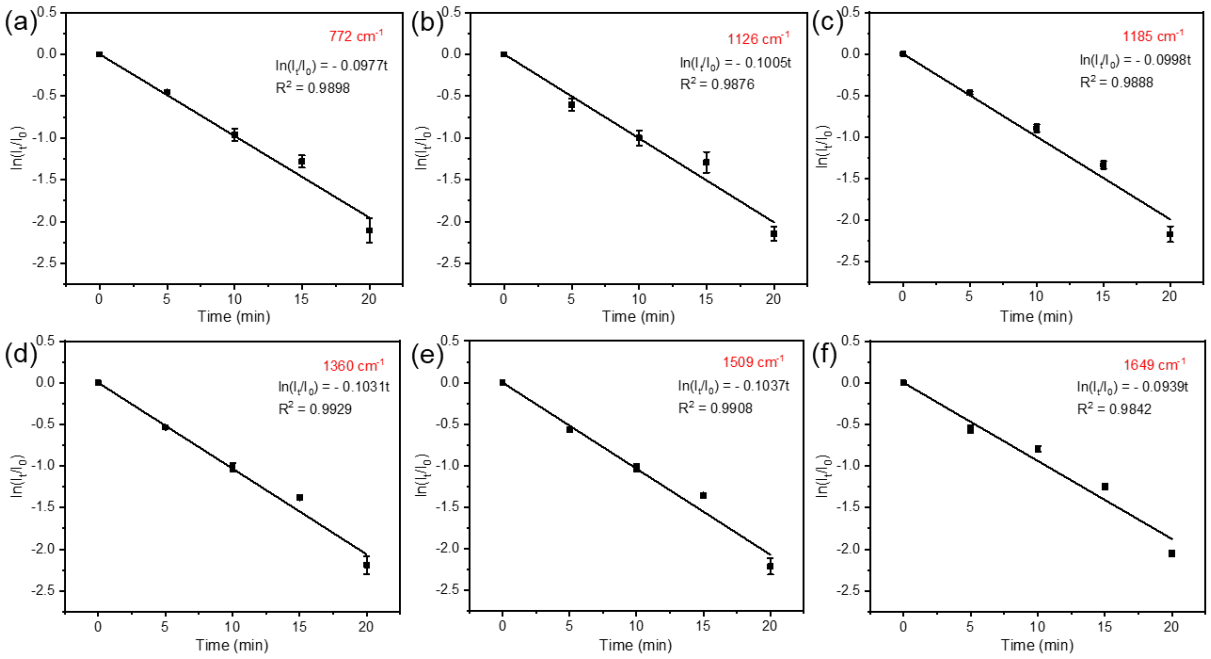

Fig. S8. (a-f) Plots of ln (I_t/I_0) versus time for the peaks at 772, 1126, 1185, 1360, 1509, and 1649 cm^{-1} during photocatalytic degradation of 1×10^{-5} M R6G on the g-C_3N_4/AuNPs nanocomposite film.

Table S2. Band assignments for the major peaks of methylene blue, acid orange II, and acid orange 74.

Organic Dyes	Raman shift (cm^{-1})	Assignments
Methylene blue [8]	466, 499	Skeletal deformation of C-N-C
	770, 1152	In-plane bending of C-H
	1395	Symmetrical stretching of C-N
	1623	Ring stretching of C-C
Acid orange II [9]	1230	Symmetrical stretching of C-N on the benzene ring and symmetrical stretching of C=C on the benzene and naphthalene rings
	1496	Symmetrical stretching of C-N and C=C, asymmetrical stretching and rocking of C-H, and rocking of C-O on the benzene ring
	1594	Non-plane rocking of C-N, in-plane rocking of C-H, and asymmetrical stretching of C-N and symmetrical stretching of C=C
Acid orange 74 [10]	520, 783	In-plane bending of C-C-C
	1037	Stretching of C-O
	1386	Stretching of C-C on the benzene ring and in-plane bending of C-H on the benzene ring

References

[1] X. Zhou, C. Zhao, J. Chen, L. Chen, Influence of B, Zn, and B-Zn doping on electronic structure and optical properties of g-C_3N_4 photocatalyst: A first-principles study, Results Phys. 26 (2021) 104338.

[2] H. Lai, H. Dai, G. Li, Z. Zhang, Rapid determination of pesticide residues in fruit and vegetable using Au@AgNPs decorated 2D Ni-MOF nanosheets as efficient surface-enhanced Raman scattering substrate, Sens. Actuators B-Chem. 369 (2022) 132360.

[3] C. Yang, Y. Yu, Y. Xie, D. Zhang, P. Zeng, Y. Dong, B. Yang, R. Liang, Q. Ou, S. Zhang, One-step synthesis of size-tunable gold nanoparticles/reduced graphene oxide nanocomposites using argon plasma and their applications in sensing, Appl. Surf. Sci. 473 (2019) 83−90.

[4] X. Hu, B. Yang, X. Wen, J. Su, B. Jia, F. Fu, Y. Zhang, Q. Yu, X. Liu, One-pot synthesis of a three-dimensional Au-decorated cellulose nanocomposite as a surface-enhanced Raman scattering sensor for selective detection and in situ monitoring, ACS Sustainable Chem. Eng. 9 (2021) 3324−3336.

[5] R. Goul, S. Das, Q. Liu, M. Xin, R. Lu, R. Hui, J. Z. Wu, Quantitative analysis of surface enhanced Raman spectroscopy of Rhodamine 6G using a composite graphene and plasmonic Au nanoparticle substrate, Carbon 111 (2017) 386–392.

[6] X. Zhang, C. Song, S. Li, L. Chen, J. Xu, W. Liu, S. Feng, Graphene-Au nanosphere composite arrays and their enhanced SERS performance, Opt. Mater. 136 (2023) 113384.

[7] G. Shi, M. Wang, Y. Zhu, L. Shen, Y. Wang, W. Ma, Y. Chen, R. Li, A flexible and stable surface-enhanced Raman scattering (SERS) substrate based on Au nanoparticles/graphene oxide/cicada wing array, Opt. Commun. 412 (2018) 28–36.

[8] C. Li, Y. Huang, K. Lai, B.A. Rasco, Y. Fan, Analysis of trace methylene blue in fish muscles using ultra-sensitive surface-enhanced Raman spectroscopy, Food Control 65 (2016) 99−105.

[9] Y. Xie, T. Chen, Y. Guo, Y. Cheng, H. Qian, W. Yao, Rapid SERS detection of acid orange II and brilliant blue in food by using Fe_3O_4@Au core–shell substrate, Food Chem. 270 (2019) 173−180.

[10] G. Vannucci, M.V. Cañamares, S. Prati, S. Sanchez-Cortes, Study of the azo-hydrazone tautomerism of acid orange 20 by spectroscopic techniques: UV–visible, Raman, and surface-enhanced Raman scattering, J. Raman Spectrosc. 51 (2020) 1295−1304.